

Van Hove singularity-induced multiple magnetic transitions in multi-orbital systems

Chen Lu^{1,*} and Lun-Hui Hu^{2,†}

¹*School of Physics and Hangzhou Key Laboratory of Quantum Matter,
Hangzhou Normal University, Hangzhou 311121, China*

²*Center for Correlated Matter and School of Physics, Zhejiang University, Hangzhou 310058, China*

Van Hove singularities (VHSs) amplify electronic correlations, providing a crucial platform for discovering novel quantum phase transitions. Here, we show that VHSs in multi-orbital systems can stabilize a variety of competing $\mathbf{Q} = 0$ magnetic orders, including intrinsic altermagnetism emerging from spontaneous orbital antiferromagnetism. This intrinsic phase, in which antiparallel spins reside on distinct orbitals, is realized across all four 2D Bravais lattices. It is driven by orbital-resolved spin fluctuations enhanced by inter-orbital hopping and favors suppressed Hund's coupling J_H , strong inter-orbital hybridization, and filling near a VHS from quadratic band touching. Through Hubbard- U - J_H phase diagrams we map several magnetic phase transitions: (i) ferrimagnet to d -wave extrinsic altermagnet, (ii) d -wave intrinsic altermagnet to ferromagnet, and (iii) g -wave extrinsic altermagnet to either d -wave extrinsic altermagnet or ferromagnet. Our work identifies VHSs as a generic route to altermagnetism in correlated materials.

Introduction

Van Hove singularities (VHSs) originate from saddle points in the electronic band structure and typically produce a logarithmic divergence in the density of states [1]. When the Fermi level lies near such a singularity, electronic correlations are strongly enhanced, making the system a fertile platform for exploring symmetry-breaking orders, including unconventional superconductivity [2–12], charge density waves [13–17], and magnetism [18–32]. In multi-orbital systems, the influence of VHSs is further enriched by orbital-selective saddle points, which can generate complex, competing magnetic orders. Thus, tuning microscopic parameters (e.g., doping, strain) can induce a redistribution of spin polarization across orbitals or sublattices, often favoring exotic compensated magnetic states over conventional ferromagnetic or Néel antiferromagnetic orders [33–36].

One prominent example of unconventional magnetism is altermagnetism, a recently identified collinear antiferromagnetic phase characterized by vanishing net magnetization and momentum-dependent spin-split electronic bands [37–47]. The altermagnetic phase has been experimentally confirmed in diverse materials [48–64], and provides promising platforms for novel spintronic functionalities [65–70]. Alternative theoretical mechanisms for non-relativistic spin-splitting, such as spin-channel Pomeranchuk instabilities [71–73] and d -wave spin-density waves [74], have also been proposed. In altermagnets, the compensated spin sublattices feature antiparallel spins that can be only interchanged via crystalline symmetries, such as rotation and reflection [65], resulting in the breaking of both composite $\mathcal{P} \cdot \mathcal{T}$ (parity-time reversal) and $t \cdot \mathcal{T}$ (translation-time reversal) symmetries [75, 76]. These characteristics give rise to various momentum-space spin textures, including d -, g -, and i -wave textures [77].

From a symmetry perspective, altermagnetism represents a distinct class of correlated phases [78]. Given its considerable potential for antiferromagnetic spintronics, numerous theoretical mechanisms for realizing altermagnetism have been proposed, including orbital ordering [79], stacking twisted van der Waals ferromagnets [80, 81], coupling to ferroelectrics [82–84], and engineering lattice vacancies [85–87]. While correlation effects are recognized as central to magnetism [88–92], the role of VHSs in driving transitions between altermagnetic and other collinear orders remains largely unexplored.

In this work, we investigate the conditions under which VHSs stabilize altermagnetic phases. Using analytical arguments and random-phase-approximation calculations, we show that inter-orbital hopping strongly enhances orbital-resolved spin fluctuations, which in turn stabilizes an altermagnetic phase emerging from orbital antiferromagnetism. This phase is favored under conditions of large Hubbard repulsion U but small Hund's coupling J_H . By computing the staggered susceptibilities for various collinear magnetic phases, we construct comprehensive U - J_H phase diagrams. These diagrams reveal rich phase competition, including transitions between extrinsic/intrinsic altermagnetism, ferromagnetism, ferrimagnetism, and Néel antiferromagnetism. Moreover, our work establishes that VHSs arising from quadratic Dirac band touching can play a central mechanism for stabilizing altermagnetism.

Symmetry classification and prototype models

We begin with a general symmetry analysis to establish orbital antiferromagnetism as a mechanism for altermagnetism in two-dimensional (2D) systems. To illustrate this, we consider a 2D Bravais lattice with a single atom per site hosting two locally degenerate (or nearly degenerate) orbitals, such as $\{p_x, p_y\}$ or $\{d_{xz}, d_{yz}\}$. The relevant point-group symmetries are C_2 for oblique lattice, C_{2v} for rectangular and centered rectangular lattice, C_{4v} for square lattice, and C_{6v} for hexagonal lattice. Inversion \mathcal{P} in this case is equivalent to C_{2z} . The combination of these

* luchen@hznu.edu.cn

† lunhui@zju.edu.cn

point groups with time-reversal symmetry \mathcal{T} governs the symmetry-breaking patterns of orbital antiferromagnetic order, and we define the orders as

$$\hat{\mathcal{O}}_1(\mathbf{r}) = c_{p_x,\uparrow}^\dagger(\mathbf{r})c_{p_x,\uparrow}(\mathbf{r}) - c_{p_x,\downarrow}^\dagger(\mathbf{r})c_{p_x,\downarrow}(\mathbf{r}) - c_{p_y,\uparrow}^\dagger(\mathbf{r})c_{p_y,\uparrow}(\mathbf{r}) + c_{p_y,\downarrow}^\dagger(\mathbf{r})c_{p_y,\downarrow}(\mathbf{r}), \quad (1)$$

$$\hat{\mathcal{O}}_2(\mathbf{r}) = c_{p_+,\uparrow}^\dagger(\mathbf{r})c_{p_+,\uparrow}(\mathbf{r}) - c_{p_+,\downarrow}^\dagger(\mathbf{r})c_{p_+,\downarrow}(\mathbf{r}) - c_{p_-,\uparrow}^\dagger(\mathbf{r})c_{p_-,\uparrow}(\mathbf{r}) + c_{p_-,\downarrow}^\dagger(\mathbf{r})c_{p_-,\downarrow}(\mathbf{r}), \quad (2)$$

where \mathbf{r} denotes the lattice site and $c_{p\pm} = (c_{p_x} \pm c_{p_y})/\sqrt{2}$ are the electron creation operators. Both $\hat{\mathcal{O}}_1(\mathbf{r})$ and $\hat{\mathcal{O}}_2(\mathbf{r})$ encode spin-orbital correlations with opposite spin polarization on distinct orbitals. We assume a long-range order such that $\langle \hat{\mathcal{O}}(\mathbf{r})\hat{\mathcal{O}}(0) \rangle$ remains finite as $r \rightarrow \infty$, and further that the order parameter $\langle \hat{\mathcal{O}}(\mathbf{r}) \rangle$ preserves the translational symmetry of the unit cell (i.e., $t \cdot \mathcal{T}$ is broken). Under these conditions, the orders $\langle \hat{\mathcal{O}}(\mathbf{r}) \rangle$ can be classified according to the groups $C_2 \otimes \mathcal{T}$, $C_{2v} \otimes \mathcal{T}$, $C_{4v} \otimes \mathcal{T}$, and $C_{6v} \otimes \mathcal{T}$ groups. In the absence of spin-orbit coupling, the symmetry of the system is described by a spin-space group. In this description, a symmetry operation $\{g_s||g_r\}$ acts independently on real space (g_r) and spin space (g_s). For example: the group $C_2 \otimes \mathcal{T}$ is generated by $\{E||C_{2z}\}$ and $\{\mathcal{T}||C_{2z}\}$, where \mathcal{T} is the spinful time-reversal operator satisfying $\mathcal{T}^2 = -1$.

Our symmetry classification, summarized in Table I, reveals that the $\{\mathcal{T}||C_{2z}\}$ symmetry (or equivalently $\mathcal{P} \cdot \mathcal{T}$) is broken in all cases, giving rise to the characteristic spin-splitting of altermagnetism. However, altermagnetism further requires a vanishing net magnetization, a condition that leads to key differences among lattice types. For any symmetry operator g , its action on the order parameter in Eqs. (1) and (2) follows $g\hat{\mathcal{O}}_{1,2}g^{-1}$. When the order parameter respects the symmetry, $g\hat{\mathcal{O}}_{1,2}g^{-1} = \hat{\mathcal{O}}_{1,2}$; conversely, if the operation changes the order parameter, the symmetry is broken, as indicated by the $-$ or \times entries in Table I. In practice, the oblique lattice cannot host altermagnetism because its antiferromagnetic order lacks the symmetry constraints needed to enforce zero net magnetization. By contrast, the \mathcal{O}_2 phase preserves $\{\mathcal{T}||C_{2x}\}$ symmetry in rectangular, centered rectangular, and square lattices, ensuring full spin compensation and realizing $d_{x^2-y^2}$ -wave altermagnetism. Meanwhile, the \mathcal{O}_1 order produces $d_{x^2-y^2}$ -wave altermagnetism only in square lattices, which will be addressed later with explicit model calculations. Because both \mathcal{O}_1 and \mathcal{O}_2 spontaneously break both $\mathcal{P} \cdot \mathcal{T}$ and $t \cdot \mathcal{T}$ symmetries, we refer to them as *intrinsic altermagnetic phase*. Moreover, in hexagonal lattices, \mathcal{O}_2 explicitly breaks C_{6z} symmetry, giving rise to a nematic altermagnetic state [93, 94].

While the symmetry-adapted analysis has focused primarily on orbital antiferromagnetism, a complete treatment must also incorporate other competing magnetic orders. These include the $\mathbf{Q} = (\pi, \pi)$ Néel order [95] (relevant for both Néel antiferromagnetism and extrinsic

TABLE I. Symmetry classification of the $\mathcal{O}_{1/2}$ orbital-AFM orders (defined in Eqs. (1) and (2)) across five Bravais lattices. (AM = altermagnet; AFM = antiferromagnet)

$C_2 \otimes \mathcal{T}$	$\{E C_{2z}\}$	$\{\mathcal{T} C_{2z}\}$	spin-splitting	magnetization	altermagnetism
$\mathcal{O}_1 \propto \tau_z S_z$	+	-	✓	✓	No
$\mathcal{O}_2 \propto \tau_z S_z$	+	-	✓	✓	No
$C_{2v} \otimes \mathcal{T}$	$\{E C_{2z}\}$	$\{\mathcal{T} C_{2z}\}$	$\{E C_{2x}\}$	$\{\mathcal{T} C_{2x}\}$	spin-splitting
$\mathcal{O}_1 \propto \tau_z S_z$	+	-	+	-	✓
$\mathcal{O}_2 \propto \tau_z S_z$	+	-	-	+	✓
$C_{4v} \otimes \mathcal{T}$	$\{E C_{4z}\}$	$\{\mathcal{T} C_{4z}\}$	$\{E C_{2x}\}$	$\{\mathcal{T} C_{2x}\}$	spin-splitting
$\mathcal{O}_1 \propto \tau_z S_z$	-	+	+	-	✓
$\mathcal{O}_2 \propto \tau_z S_z$	-	+	-	+	✓
$C_{6v} \otimes \mathcal{T}$	$\{E C_{6z}\}$	$\{\mathcal{T} C_{6z}\}$	$\{E C_{2x}\}$	$\{\mathcal{T} C_{2x}\}$	spin-splitting
$\mathcal{O}_1 \propto \tau_z S_z$	X	X	+	-	✓
$\mathcal{O}_2 \propto \tau_z S_z$	X	X	-	+	✓

altermagnetism), ferromagnetic order, and ferrimagnetic order. These distinct phases typically emerge in different parameter regimes of correlated systems. To systematically identify altermagnetism in competition with these phases, we study the minimal two-orbital Hubbard model on a square lattice. As illustrated in Fig. 1(a), the system contains two sublattices (labeled with A and B) per unit cell, each hosting two degenerate orbitals (e.g., d_{xz} and d_{yz}). Our Hamiltonian treats both the limiting case of equivalent sublattices ($A = B$) and the general case with broken sublattice-inversion symmetry. The tight-binding model is given by

$$H_{tb}(\mathbf{k}) = \tau_0 [\epsilon_0(\mathbf{k})\sigma_0 + \text{Re}[\epsilon_1(\mathbf{k})]\sigma_x - \text{Im}[\epsilon_1(\mathbf{k})]\sigma_y + \epsilon_3(\mathbf{k})\sigma_z] + [f_1(\mathbf{k})\tau_x + f_3(\mathbf{k})\tau_z]\sigma_0, \quad (3)$$

where $\epsilon_0(\mathbf{k}) = -(t_1 + t_2)[\cos(k_x + k_y) + \cos(k_x - k_y)] - \mu$ with μ the chemical potential, $\epsilon_1(\mathbf{k}) = -t_0[1 + e^{ik_x} + e^{ik_y} + e^{i(k_x+k_y)}]$, $\epsilon_3(\mathbf{k}) = (t_2 - t_1)[\cos(k_x + k_y) - \cos(k_x - k_y)]$, $f_1(\mathbf{k}) = -2t_3(\cos k_x - \cos k_y)$, $f_3(\mathbf{k}) = 2t_5[\cos(k_x + k_y) - \cos(k_x - k_y)]$, and $\tau_{x,y,z}$ and $\sigma_{x,y,z}$ are Pauli matrices acting on the orbital and sublattice degrees of freedom, respectively. These hopping parameters are illustrated in Fig. 1(a). Among them, $\{t_0, t_1, t_2\}$ are orbital-independent, while $\{t_3, t_5\}$ are orbital-dependent. We set $t_0 = 1$ as the energy unit of the system. In this work, we consider both the case where $t_1 = t_2$ (corresponding to identical A and B sublattices, i.e., the 1×1 square lattice) and another case with $t_1 \neq t_2$ (i.e., the $\sqrt{2} \times \sqrt{2}$ square lattice). Both cases are crucial for the emergence of altermagnetic phases. For instance, the $\mathbf{Q} = (\pi, \pi)$ Néel antiferromagnetic order yields altermagnetic spin-splitting bands only in the $t_1 \neq t_2$ case [88]. We refer to this as *extrinsic altermagnetic phase*. This mechanism, in fact, describes the majority of recently discovered altermagnetic materials [96].

In the non-interacting case, Fig. 1(b) and (c) show the band structures for $t_1 = t_2$ and $t_1 \neq t_2$, respectively. In both scenarios, the chemical potential is aligned near VHS at the \mathbf{M} point. This choice enables a direct examination of correlation effects. The repulsive Hubbard-

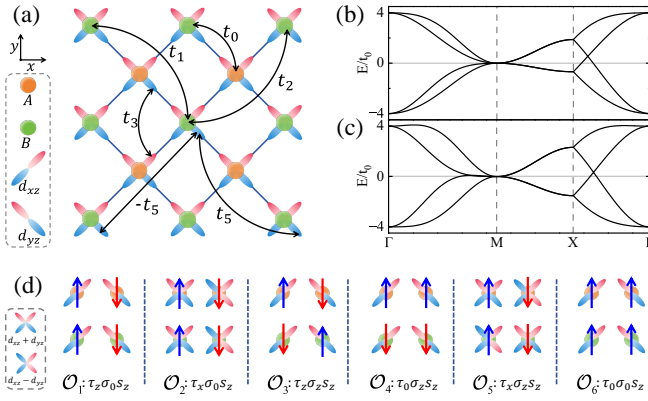


FIG. 1. Competing magnetic orders in a two-orbital square lattice model. (a) Schematic of the square lattice with two orbitals (d_{xz} , d_{yz}) and A (orange) and B (green) sublattices. Hopping parameters include intra-orbital terms (t_0, t_1, t_2) and inter-orbital terms (t_3, t_5). (b) Tight-binding band structure with parameters $\{t_0, t_1, t_2, t_3, t_5\} = \{1, 0.05, 0.05, 0.48, 0.29\}$. Gray line is $\mu = -0.19$. (c) Tight-binding band structure with parameters $\{t_0, t_1, t_2, t_3, t_5\} = \{1, 0.1, 0.05, 0.32, 0.13\}$. Gray line is $\mu = -0.3$. (d) Six possible $\mathbf{Q} = \mathbf{0}$ magnetic order configurations within a unit cell, where blue (\uparrow) and red (\downarrow) arrows represent the spin polarization of magnetic moments.

Hund interaction is,

$$H_{int} = U \sum_{\mathbf{i}, \tau} n_{\mathbf{i}\tau\uparrow} n_{\mathbf{i}\tau\downarrow} + V \sum_{\mathbf{i}s, s'} n_{\mathbf{i}, x, s} n_{\mathbf{i}, y, s'} + J_H \sum_{\mathbf{i}} \sum_{s, s'} c_{\mathbf{i}, x, s}^\dagger c_{\mathbf{i}, y, s'}^\dagger c_{\mathbf{i}, x, s'} c_{\mathbf{i}, y, s} + J_H \sum_{\mathbf{i}} c_{\mathbf{i}, x, \uparrow}^\dagger c_{\mathbf{i}, x, \downarrow}^\dagger c_{\mathbf{i}, y, \downarrow} c_{\mathbf{i}, y, \uparrow} + h.c., \quad (4)$$

where $c_{\mathbf{i}, \tau, s}$ is the electron annihilation operator at site \mathbf{i} with orbital τ and spin s , $n_{\mathbf{i}\tau s} = c_{\mathbf{i}, \tau, s}^\dagger c_{\mathbf{i}, \tau, s}$ is the corresponding density operator, $\tau = \{x, y\}$ labels the $\{d_{xz}, d_{yz}\}$ orbitals, and $s = \{\uparrow, \downarrow\}$ denotes the spin. Here, U is the intra-orbital Hubbard interaction, V is the inter-orbital Hubbard term, and J_H is the Hund's coupling. The spin rotation symmetry imposes the constraint $U = V + 2J_H$ [97]. Then, we treat U and J_H/U as tuning parameters to explore both *intrinsic* and *extrinsic* altermagnetic phases, as well as their transitions to other magnetic orders.

Based on Eq. (4), one can find that \mathcal{O}_1 originates from the mean-field decomposition of both U and V terms, whereas \mathcal{O}_2 emerges from the J_H term. Their matrix representations are given by

$$\mathcal{O}_1 \triangleq \tau_z \sigma_0 s_z \text{ and } \mathcal{O}_2 \triangleq \tau_x \sigma_0 s_z, \quad (5)$$

where s_z denotes the spin Pauli matrix. Furthermore, the $U-V-J_H$ interactions permit three collinear-type stag-

TABLE II. Summary of the six $\mathbf{Q} = \mathbf{0}$ magnetic phases $\mathcal{O}_1 \rightarrow \mathcal{O}_6$ defined in the unit-cell basis corresponding to the $\sqrt{2} \times \sqrt{2}$ lattice. Abbreviations: iAM = intrinsic altermagnetism; AFM = antiferromagnetism; FerriM = ferrimagnetism; eAM = extrinsic altermagnetism; FM = ferromagnetism.

orders	\mathcal{O}_1	\mathcal{O}_2	\mathcal{O}_3	\mathcal{O}_4	\mathcal{O}_5	\mathcal{O}_6
$t_1 = t_2$	iAM	iAM	AFM	AFM	AFM	FM
$t_1 \neq t_2$	iAM	iAM	FerriM	<i>d</i> -wave eAM	<i>g</i> -wave eAM	FM

gered orders ($\mathcal{O}_{3,4,5}$) and ferromagnetic order (\mathcal{O}_6),

$$\begin{aligned} \mathcal{O}_3 &\triangleq \tau_z \sigma_z s_z \text{ and } \mathcal{O}_4 \triangleq \tau_0 \sigma_z s_z, \\ \mathcal{O}_5 &\triangleq \tau_x \sigma_z s_z \text{ and } \mathcal{O}_6 \triangleq \tau_0 \sigma_0 s_z. \end{aligned} \quad (6)$$

In this work, we focus on both *intrinsic* and *extrinsic* altermagnetic phases, where $\mathbf{Q} = \mathbf{0}$ serves as a necessary (though not sufficient) condition. This constraint limits the competing orders to the $\mathcal{O}_{1 \rightarrow 6}$ phases. The corresponding real-space spin configuration, displayed in Fig. 1(d), features antiparallel magnetic moments represented by blue (\uparrow) and red (\downarrow) arrows.

Before proceeding with calculations, we present a symmetry analysis of the staggered orders ($\mathcal{O}_{1 \rightarrow 5}$). When $t_1 = t_2$, the 1×1 square lattice preserves the C_{4v} point group symmetry. Based on Table I, both \mathcal{O}_1 and \mathcal{O}_2 correspond to intrinsic *d*-wave altermagnetism. In contrast, the remaining three orders ($\mathcal{O}_{3/4/5}$) involve the σ_z matrix, which spontaneously enlarges the magnetic unit cell from 1×1 to $\sqrt{2} \times \sqrt{2}$, analogous to the conventional Néel order. Owing to the combined parity-time symmetry $\mathcal{P} \cdot \mathcal{T}$, where \mathcal{P} swaps sublattices A and B, these three orders *cannot* produce spin-split bands. Consequently, $\mathcal{O}_{1/2}$ and $\mathcal{O}_{3/4/5}$ belong to distinct symmetry representations. However, \mathcal{P} can be broken in the non-interacting Hamiltonian, for instance, by setting $t_1 \neq t_2$, as used in this work. Such a term can originate from non-magnetic atoms [88], lattice strain [85] or Jahn-Teller distortion [98], thereby enlarging the crystalline unit cell to $\sqrt{2} \times \sqrt{2}$. This breaking of \mathcal{P} enables extrinsic spin-splitting bands in $\mathcal{O}_{3/4/5}$ phases. In particular, both \mathcal{O}_4 and \mathcal{O}_5 exhibit zero net magnetization and realize extrinsic altermagnetism, whereas \mathcal{O}_3 breaks all the symmetries required for antiferromagnetic classification and instead shows characteristics of a ferrimagnetic state. We summarize these analysis in Table II.

Symmetry-breaking magnetic instabilities

To analyze magnetic instabilities, we employ the standard multi-orbital random-phase approximation (RPA) approach [99–102]. RPA has been extensively applied to conventional Néel and ferromagnetic orders. The bare susceptibility tensor in momentum space is defined as,

$$\begin{aligned} [\chi^{(0)}(\mathbf{k}, \tau)]_{l_3 l_4}^{l_1 l_2} &\equiv \frac{1}{N} \sum_{\mathbf{k}_1 \mathbf{k}_2} \langle T_\tau c_{l_1}^\dagger(\mathbf{k}_1, \tau) c_{l_2}(\mathbf{k}_1 + \mathbf{k}, \tau) \\ &\times c_{l_3}^\dagger(\mathbf{k}_2 + \mathbf{k}, 0) c_{l_4}(\mathbf{k}_2, 0) \rangle_0, \end{aligned} \quad (7)$$

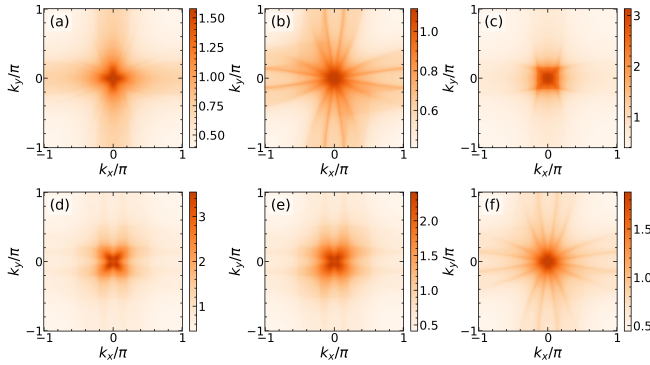


FIG. 2. Momentum-space distribution of RPA susceptibilities $\chi_{\alpha}^{\text{RPA}}(\mathbf{k})$. (a-f) Calculated susceptibility $\chi_{1\rightarrow 6}^{\text{RPA}}(\mathbf{k})$ for $U = 1$ and $J_H = 0.2$. The \mathcal{O}_4 phase (panel d) exhibits the strongest susceptibility with pronounced peaks at the Γ point (slightly exceeding that of the \mathcal{O}_3 phase in panel c). All calculations use the same parameters as in Fig. 1(c).

where $\langle \dots \rangle_0$ denotes the thermal average for the non-interacting system, N is the lattice size, τ is imaginary time, T_{τ} is the imaginary time-ordering operator, and $l_1, l_2, l_3, l_4 \in \{1, 2, 3, 4\}$ are sublattice-orbital indices corresponding to the basis states $\{|A, d_{xz}\rangle, |A, d_{yz}\rangle, |B, d_{xz}\rangle, |B, d_{yz}\rangle\}$. The complete computational formulation for Eq. (7) is provided in Methods, where we perform Fourier transformation on τ and work on the Matsubara frequency ($i\omega_n$) domain. The spin-orbit coupling is excluded in this work, and consequently, the electron operator in Eq. (7) is spin-independent (i.e., carries no explicit spin index). We emphasize that the Hamiltonian in Eq. (3) is expressed in the unit-cell gauge. Therefore, $[\chi^{(0)}(\mathbf{k}, i\omega_n)]_{l_1 l_2}^{l_3 l_4}$ having its maximum at $\mathbf{k} \neq 0$ indicates breaking of the unit-cell translational symmetry. However, the magnetic orders $\mathcal{O}_{1\rightarrow 6}$ defined above preserve this translational symmetry and consequently must appear at $\mathbf{k} = 0$. All relevant information can be extracted from the bare susceptibility tensor $[\chi^{(0)}(\mathbf{k}, i\omega_n)]_{l_3 l_4}^{l_1 l_2}$. In particular, the static bare susceptibilities for $\mathcal{O}_{1\rightarrow 6}$ are given by

$$\chi_{\alpha}^{(0)}(\mathbf{k}) = \frac{1}{2} \sum_{l_1 l_2 l_3 l_4} [\bar{\mathcal{O}}_{\alpha}]_{l_1 l_2} [\bar{\mathcal{O}}_{\alpha}]_{l_3 l_4} [\chi^{(0)}]_{l_3 l_4}^{l_1 l_2}, \quad (8)$$

where $\chi^{(0)} \equiv \chi^{(0)}(\mathbf{k}, i\omega_n = 0)$ and $\bar{\mathcal{O}}_{\alpha}$ encode the orbital-sublattice components of the corresponding order parameters \mathcal{O}_{α} [Eqs. (5) and (6)], given by: $\bar{\mathcal{O}}_{1\rightarrow 6} = \{\tau_z \sigma_0, \tau_x \sigma_0, \tau_z \sigma_z, \tau_0 \sigma_z, \tau_x \sigma_z, \tau_0 \sigma_0\}$. To realize the intrinsic altermagnetism ($\mathcal{O}_{1/2}$), we scan the band parameter space within physically plausible limits. In Sec. A of Supplementary Material (SM), we present $\chi_{\alpha}^{(0)}(\mathbf{k})$ along high-symmetry lines and identify the leading magnetic instability. For the band parameters adopted in Fig. 1(b), the \mathcal{O}_1 (intrinsic altermagnetism) order dominates, whereas for those in Fig. 1(c), the \mathcal{O}_3 (ferrimagnetism) order becomes the most relevant instability. In addition, intrinsic altermagnetic order is obtained over a

wide range of parameters [see Sec. B of SM].

We now introduce the interactions in Eq. (4) to determine whether \mathcal{O}_1 and \mathcal{O}_3 remain the leading instabilities in the interacting system. Within the RPA framework, repulsive onsite Hubbard interactions suppress charge susceptibility while enhancing spin susceptibility [99]. Specifically, the RPA-renormalized static susceptibility for the \mathcal{O}_{α} order takes the form

$$\chi_{\alpha}^{\text{RPA}}(\mathbf{k}) = \frac{1}{2} \sum_{l_1 l_2 l_3 l_4} [\bar{\mathcal{O}}_{\alpha}]_{l_1 l_2} [\bar{\mathcal{O}}_{\alpha}]_{l_3 l_4} [\chi_{\text{spin}}^{\text{RPA}}]_{l_3 l_4}^{l_1 l_2}, \quad (9)$$

where $\chi_{\text{spin}}^{\text{RPA}} \equiv \chi_{\text{spin}}^{\text{RPA}}(\mathbf{k}, i\omega_n = 0)$ denotes the spin susceptibility tensor. It is obtained through the Dyson equation, $\chi_{\text{spin}}^{\text{RPA}}(\mathbf{k}, 0) = [I - \chi^{(0)}(\mathbf{k}, 0)U^{(s)}]^{-1}\chi^{(0)}(\mathbf{k}, 0)$, where I denotes the identity matrix and $U^{(s)}$ the interaction matrix in the spin channel [see Methods]. Then, Eq. (9) allows us to compare the susceptibility channels for different competing orders. In general, the spin susceptibility tensor $[\chi_{\text{spin}}^{\text{RPA}}(\mathbf{k}, 0)]_{l_3 l_4}^{l_1 l_2}$ diverges at a critical interaction strength U_c and at an ordering wavevector \mathbf{Q} . Here, U_c determines the magnetic/non-magnetic phase boundary and \mathbf{Q} characterizes the spatial periodicity of the dominant magnetic phase. For $U > U_c$, the system develops long-range magnetic order. The magnetic phase transition is driven by the divergence of $[\chi_{\text{spin}}^{\text{RPA}}]_{l_3 l_4}^{l_1 l_2}$ at U_c , which simultaneously triggers the divergence of $\chi_{\alpha}^{\text{RPA}}$.

We use the shorthand $\chi_{\Gamma, \alpha}^{\text{RPA}} \equiv \chi_{\alpha}^{\text{RPA}}(\Gamma)$ for notational simplicity. We first examine the case where \mathcal{O}_3 is the leading instability at $U = J_H = 0$, using the band parameters of Fig. 1(c). Based on Eq. (9), Figure 2 presents the calculated momentum-resolved RPA susceptibility $\chi_{\alpha}^{\text{RPA}}(\mathbf{k})$ for $U = 1$ and $J_H = 0.2$. We find that the dominant susceptibility channel, $\chi_4^{\text{RPA}}(\mathbf{k})$, exhibits a pronounced peak at the Γ point. This indicates that, after interaction renormalization, the \mathcal{O}_4 order (extrinsic altermagnetism) becomes the leading instability, rather than \mathcal{O}_3 . The resulting magnetic phase transition from \mathcal{O}_3 to \mathcal{O}_4 occurs at weak interaction strengths due to the electron filling being near the VHS.

To systematically explore the magnetic phase transitions, we construct interaction phase diagrams in the $U-J_H$ plane for systems exhibiting *intrinsic* or *extrinsic* altermagnetism. Our approach involves three steps: (i) identifying parameter sets that maximize $\chi_{\alpha}^{\text{RPA}}(\mathbf{k})$ at the Γ -point for the target \mathcal{O}_{α} order, (ii) determining the critical interaction strength U_c ; and (iii) identifying the dominant magnetic orders near criticality. Specific examples are presented in the following three cases.

Case I: phase diagram with d -wave extrinsic altermagnetism. In our previous calculations, we set $U = 1$ and $J_H = 0.2$ for Fig. 2. We then construct the $U-J_H$ phase diagram in Fig. 3(a), which shows a transition from \mathcal{O}_3 at low J_H to \mathcal{O}_4 above a critical ratio $J_H/U = 0.114$. The solid black curve marks the boundary between non-magnetic and magnetic states, tracing U_c as a function of J_H/U . We emphasize that the \mathcal{O}_4 phase is a d -wave extrinsic altermagnet, while the \mathcal{O}_3 phase is a spin-split

ferrimagnet. These two orders are unambiguously distinguished through two methods: (i) the eigen-analysis of the spin susceptibility matrix $[\chi_{\text{spin}}^{\text{RPA}}(\Gamma, 0)]_{l_1 l_2}^{l_1 l_2}$ yields the two dominant eigenvalues $\lambda_{\mathcal{O}_3}$ and $\lambda_{\mathcal{O}_4}$, whose difference change sign at $J_H/U = 0.114$ [Fig. 3(b)]; and (ii) the comparison of divergence rates via the susceptibility difference $\chi_{\Gamma,3}^{\text{RPA}} - \chi_{\Gamma,4}^{\text{RPA}}$ [Figs. 3(c) and (d)]. Applying the same analysis procedure to the parameter set $\{t_0, t_1, t_2, t_3, t_5, \mu\} = \{1, 0.42, 0.08, 0.7, 0.49, -1\}$, we find that increasing J_H drives a transition from \mathcal{O}_3 into a ferromagnetic phase (\mathcal{O}_6 , gray) [Fig. 3(e)]. Between the two methods, the second approach—relying on the susceptibility difference—is computationally simpler. Further technical details are provided in the Methods section.

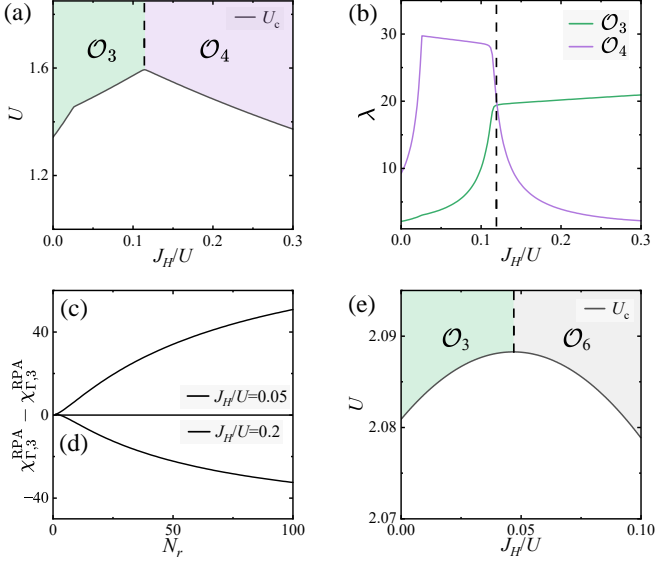


FIG. 3. The phase diagram with d -wave extrinsic altermagnetic phase [Case I]. (a) The U – J_H phase diagram for parameters used in Fig. 1(c) shows: extrinsic d -wave altermagnetic phase (\mathcal{O}_4 , purple), ferrimagnetic phase (\mathcal{O}_3 , green), and non-magnetic phase (white). The magnetic-to-non-magnetic boundary is marked by the critical U_c (solid black curve); the dashed line at $J_H/U = 0.114$ separates the \mathcal{O}_3 and \mathcal{O}_4 phases. (b) The two largest eigenvalues of the susceptibility matrix correspond to the \mathcal{O}_3 and \mathcal{O}_4 phases. (c,d) Divergence of the susceptibility difference $\chi_{\Gamma,1}^{\text{RPA}} - \chi_{\Gamma,6}^{\text{RPA}}$ as U approaches U_c , with $U = (1 - 1/N_r)U_c$ and N_r running from 0 to 200. Results are shown for $J_H/U = 0.05$ (c) and $J_H/U = 0.2$ (d). All calculations employ the band parameters of Fig. 1(c). (e) The transition between \mathcal{O}_3 and \mathcal{O}_6 occurs at $J_H/U = 0.047$. Parameters: $\{t_0, t_1, t_2, t_3, t_5, \mu\} = \{1, 0.42, 0.08, 0.7, 0.49, -1\}$.

Case II: phase diagram with d -wave intrinsic altermagnetism. Using the band parameters in Fig. 1(b), where the inter-orbital hopping parameters t_3 and t_5 are enhanced relative to those in Fig. 1(a) [Case I], we obtain the full phase diagram in the U – J_H/U plane shown in Fig. 4(a). The phase diagram consists of two distinct magnetic states: d -wave intrinsic altermagnetism (\mathcal{O}_1 , blue), and ferromagnetism (\mathcal{O}_6 , gray). Hund’s coupling naturally favors parallel spin alignment across

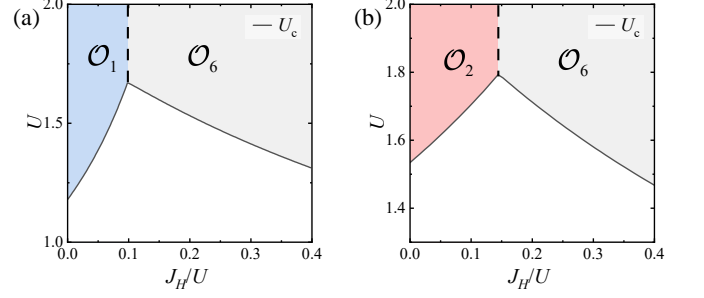


FIG. 4. The phase diagram with d -wave intrinsic altermagnetic phase [Case II]. (a) The phase diagram for parameters used in Fig. 1(b) shows: intrinsic d -wave altermagnetic phase (\mathcal{O}_1 , blue), ferromagnetic phase (\mathcal{O}_6 , gray), and non-magnetic phase (white). The dashed line separates the \mathcal{O}_1 and \mathcal{O}_6 phases at $J_H/U = 0.098$. The parameters are the same as Fig. 1(b). (b) Similarly, using another set of band parameters leads to the other intrinsic altermagnetic phase (\mathcal{O}_2 , red). The phase boundary between \mathcal{O}_2 and \mathcal{O}_6 is $J_H/U = 0.144$. Parameters: $\{t_0, t_1, t_2, t_3, t_5, \mu\} = \{1, 0.25, 0.25, 0.17, 0.07, -1\}$.

orbitals, which stabilizes the \mathcal{O}_6 phase at larger J_H . Moreover, for the parameter set $\{t_0, t_1, t_2, t_3, t_5, \mu\} = \{1, 0.25, 0.25, 0.17, 0.07, -1\}$, we identify an additional intrinsic altermagnetic phase \mathcal{O}_2 (red), which emerges over a broader range of J_H [Fig. 4(b)]. Further details on the modified Stoner ferromagnetism and the altermagnetic fluctuation-induced spin-triplet superconductivity can be found in Refs. [103, 104].

Case III: phase diagram with g -wave extrinsic altermagnetism. We now employ a different parameter set $\{t_0, t_1, t_2, t_3, t_5, \mu\} = \{1, 0.1, 0.05, 0.14, 0.2, -0.26\}$, which maintains filling near the VHSs but reduces t_3 and enhances t_5 relative to the Case I. This leads to a distinct J_H -driven transition between two extrinsic altermagnetic phases: a g -wave phase (\mathcal{O}_5 , brown) at low J_H and a d -wave phase (\mathcal{O}_4 , purple) at large J_H

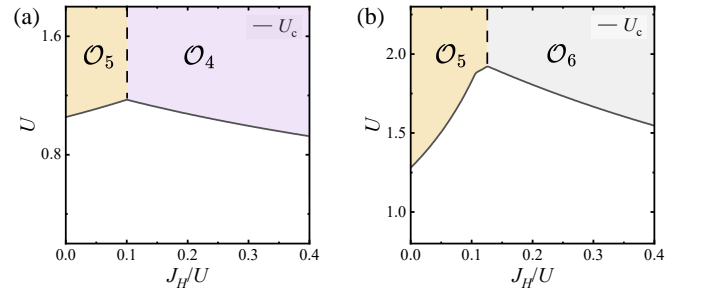


FIG. 5. The phase diagram with g -wave extrinsic altermagnetic phase [Case III]. (a) Phase diagram includes extrinsic g -wave altermagnetic phase (\mathcal{O}_5 , brown), extrinsic d -wave altermagnetic phase (\mathcal{O}_4 , purple), and non-magnetic phase (white). The transition between \mathcal{O}_5 and \mathcal{O}_4 occurs at $J_H/U = 0.1$. Parameters: $\{t_0, t_1, t_2, t_3, t_5, \mu\} = \{1, 0.1, 0.05, 0.14, 0.2, -0.26\}$. (b) shows the transition from \mathcal{O}_5 to \mathcal{O}_6 at $J_H/U = 0.126$. Parameters: $\{t_0, t_1, t_2, t_3, t_5, \mu\} = \{1, 0.1, 0.05, 0.36, 0.32, -0.08\}$.

[Fig. 5(a)], in qualitative agreement with mean-field results [98]. Moreover, a magnetic phase transition from \mathcal{O}_5 to a ferromagnetic phase (\mathcal{O}_6 , gray) is also observed in Fig. 5(b), where we use another parameter set, $\{t_0, t_1, t_2, t_3, t_5, \mu\} = \{1, 0.1, 0.05, 0.36, 0.32, -0.08\}$.

Discussions and conclusion

Tunable magnetic phase transitions. The three cases presented above demonstrate that the magnetic phase transitions are highly tunable, governed by both the kinetic energy (hopping parameters) and the interaction strengths (U and J_H). Here, we summarize all possible transitions among the \mathcal{O}_{1-6} phases in a two-orbital system [Fig. 6]. Larger Hund's coupling J_H generally favors either the d -wave extrinsic altermagnet \mathcal{O}_4 or the ferromagnetic phase \mathcal{O}_6 , whereas reducing J_H can drive the system toward the remaining four phases ($\mathcal{O}_{1,2,3,5}$). Transitions among these four are further mediated by variations in the hopping parameters. For instance, comparing Fig. 4(b) [Case II] with Fig. 5(b) [Case III] shows that a transition from the d -wave intrinsic altermagnet \mathcal{O}_1 to the g -wave extrinsic altermagnet \mathcal{O}_5 can be realized by decreasing $t_{1,2}$ while increasing $t_{3,5}$. More details are provided in Sec. D of SM. Although a full $t-U-J_H$ phase diagram is beyond the scope of this work, the results presented here serve as essential building blocks for understanding the rich landscape of VHS-induced multiple magnetic phase transitions.

Role of VHS. The $\mathbf{Q} = \mathbf{0}$ orders emerge precisely as the chemical potential approaches the VHS, highlighting its crucial role. Since $\mathbf{Q} = \mathbf{0}$ is a necessary requirement for both *extrinsic* and *intrinsic* altermagnetism, we examine the VHS influence below. In Eq. (10), we note that while the normalized eigenvector product contribution remains finite, the Lindhard function term $[\eta_F(\varepsilon_{\mathbf{k}_1+\mathbf{Q}}^\beta) - \eta_F(\varepsilon_{\mathbf{k}_1}^\alpha)]/[\varepsilon_{\mathbf{k}_1}^\alpha - \varepsilon_{\mathbf{k}_1+\mathbf{Q}}^\beta]$ can diverge. At low temperature, this divergence at $\mathbf{Q} = \mathbf{0}$ requires three simultaneous conditions: (1) a finite numerator, requiring that the α and β bands to be on opposite sides of the Fermi level (one occupied, one unoccupied); (2) a vanishing denominator, demanding both band energies approach the Fermi level; and (3) a sufficiently high density of states (DOS) at \mathbf{k}_1 -points where conditions (1) and (2) are simultaneously satisfied, ensuring the integrated susceptibility yields a strong divergence. Therefore, the condition (3) is automatically satisfied when the Fermi level is tuned near a VHS at high-symmetry points, implying the band structure must exhibit a Dirac semi-metal character (e.g., $\epsilon_\alpha \sim k^2$ and $\epsilon_\beta \sim -k^2$). This is directly confirmed by Figs. 1(b) and (c).

We next show that these conditions maximize the susceptibility at $\mathbf{Q} = \mathbf{0}$. As the Fermi level approaches a VHS, a set of high-DOS “hot spots” emerges in momentum space. To identify the dominant instability, it suffices to examine the nesting vectors connecting these hot spots, which include both $\mathbf{Q} \neq \mathbf{0}$ (inter-VHS) and $\mathbf{Q} = \mathbf{0}$ (intra-VHS). When the VHS is located near a single high-symmetry point (e.g., \mathbf{F} , \mathbf{M} , \mathbf{X} , \dots), $\mathbf{Q} = \mathbf{0}$ is the only

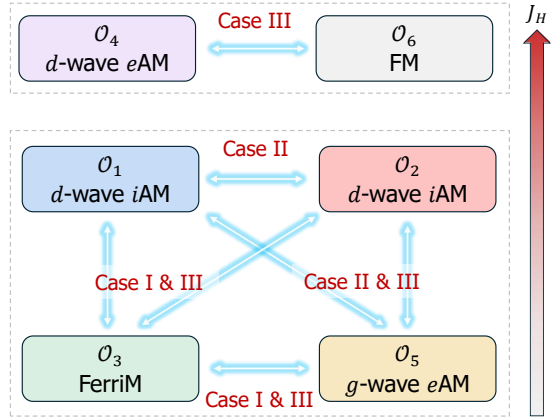


FIG. 6. A summary of this work: tunable magnetic phase transitions for the six $\mathbf{Q} = \mathbf{0}$ orders \mathcal{O}_{1-6} [see Table II].

nesting vector capable of linking them. Moreover, the band degeneracy at VHS points is typically symmetry-protected, the $\mathbf{Q} = \mathbf{0}$ order inherits this protection, enhancing its stability against perturbations.

In the general case where multiple VHSs lie away from high-symmetry points, both inter-VHS and intra-VHS nesting contributions coexist. The intra-VHS typically dominates in the Lindhard function part. For instance, consider two VHSs located at \mathbf{q}_1 and \mathbf{q}_2 with semi-metal dispersions $\epsilon(\mathbf{k} - \mathbf{q}_1) = \pm t_1 k^2$ and $\epsilon(\mathbf{k} - \mathbf{q}_2) = \pm t_2 k^2$, respectively. The intra-VHS contribution to the Lindhard function scales as $1/(2t_1 k^2) + 1/(2t_2 k^2)$, while the inter-VHS term varies as $2/(t_1 k^2 + t_2 k^2)$. Consequently, as $k \rightarrow 0$, the intra-VHS divergence rate $1/2t_1 + 1/2t_2$ exceeds the inter-VHS rate $2/(t_1 + t_2)$ by the harmonic-arithmetic mean inequality. When additional VHSs are present, inter-VHS nesting produces multiple nonzero \mathbf{Q} vectors that inherently access reduced phase space compared to the intra-VHS case. Therefore, in semi-metal systems with Fermi levels near VHSs, the susceptibility consistently peaks at $\mathbf{Q} = \mathbf{0}$. Furthermore, slightly shifting the filling away from the VHSs causes the RPA susceptibilities to rapidly shift their divergence to nonzero \mathbf{Q} , as detailed in the Sec. C of SM.

Possible candidates. The above argument provides a practical guidance for realizing altermagnetism in multi-orbital quantum materials. Promising candidate systems include transition metal oxides where orbital order coexists with antiferromagnetism, such as: α -Sr₂CrO₄ with a $3d^2$ electronic configuration in the Cr⁴⁺ state [105, 106]; SrRuO₃ thin films with SrO termination [107]; various vanadium-based oxides such as V₂O₃ [108], ZnV₂O₄ [109]; and a class of manganites exhibiting robust orbital ordering, including Mn₂OBO₃ [110], Pr_{1-x}Ca_xMnO₃ [111], La_{0.5}Sr_{1.5}MnO₄ [112], and La_{0.5}Ca_{0.5}MnO₃ [113]. These orbital-active magnetic materials may provide a platform to explore various kinds of altermagnetic phases, including intrinsic altermagnetism.

Conclusion. This work establishes a universal mechanism for realizing intrinsic altermagnetism in correlated multi-orbital systems, driven by orbital antiferromagnetism with antiparallel spins locked to distinct orbitals. Using symmetry analysis and random-phase-approximation calculations, we identify the essential criteria: suppressed Hund's coupling, dominant interorbital hopping, and electron filling near Van Hove singularities from quadratic band touching. Phase diagrams in the Hubbard $U-J_H$ plane reveal rich magnetic competition, including phase transitions between intrinsic altermagnetism, extrinsic altermagnetism, ferromagnetism, and ferrimagnetism. Our results provide a clear theoretical pathway for designing altermagnetic states in correlated materials through manipulation of electronic structure and correlations.

Methods

The Multi-Orbital RPA Approach

The explicit formulism of $\chi^{(0)}$ in the momentum-frequency space is,

$$[\chi^{(0)}(\mathbf{k}, i\omega)]_{l_3 l_4}^{l_1 l_2} \equiv \frac{1}{N} \sum_{\mathbf{k}_1 \alpha \beta} [\xi_{l_1}^{\alpha}(\mathbf{k}_1)]^* \xi_{l_2}^{\beta}(\mathbf{k}_1 + \mathbf{k}) \times [\xi_{l_3}^{\beta}(\mathbf{k}_1 + \mathbf{k})]^* \xi_{l_4}^{\alpha}(\mathbf{k}_1) \frac{\eta_F(\varepsilon_{\mathbf{k}_1 + \mathbf{k}}^{\beta}) - \eta_F(\varepsilon_{\mathbf{k}_1}^{\alpha})}{i\omega + \varepsilon_{\mathbf{k}_1}^{\alpha} - \varepsilon_{\mathbf{k}_1 + \mathbf{k}}^{\beta}}, \quad (10)$$

where $\alpha, \beta \in \{1, 2, 3, 4\}$ are band indices, $\varepsilon_{\mathbf{k}}^{\alpha}$ and $\xi^{\alpha}(\mathbf{k})$ are the α -th eigenvalue and eigenvector of $H_{tb}(\mathbf{k})$ given by Eq. (3), respectively, and η_F is the Fermi-Dirac distribution function. In our calculations, a lattice size of $N = 200 \times 200$ is employed. To enhance the smoothness of the results and reduce the influence of finite-size effects, we set the temperature to 0.005. This temperature is sufficiently low to ensure that our conclusions remain unaffected by thermal fluctuations.

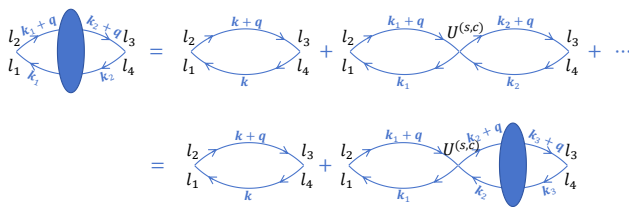


FIG. 7. Feynman's diagram for the renormalized spin/charge susceptibility in the RPA level.

When the interactions in Eq. (4) are turned on, the spin and charge susceptibilities are defined as,

$$[\chi_{\text{spin}}(\mathbf{k}, \tau)]_{l_3 l_4}^{l_1 l_2} \equiv \frac{1}{2N} \sum_{\mathbf{k}_1 \mathbf{k}_2} \sum_{ss'} \langle T_{\tau} c_{l_1, s}^{\dagger}(\mathbf{k}_1, \tau) c_{l_2, s}(\mathbf{k}_1 + \mathbf{k}, \tau) c_{l_3, s'}^{\dagger}(\mathbf{k}_2 + \mathbf{k}, 0) c_{l_4, s'}(\mathbf{k}_2, 0) \rangle, \quad (11)$$

and

$$[\chi_{\text{charge}}(\mathbf{k}, \tau)]_{l_3 l_4}^{l_1 l_2} \equiv \frac{1}{2N} \sum_{\mathbf{k}_1 \mathbf{k}_2} \sum_{ss'} \langle T_{\tau} c_{l_1, s}^{\dagger}(\mathbf{k}_1, \tau) c_{l_2, s}(\mathbf{k}_1 + \mathbf{k}, \tau) c_{l_3, s'}^{\dagger}(\mathbf{k}_2 + \mathbf{k}, 0) c_{l_4, s'}(\mathbf{k}_2, 0) \rangle, \quad (12)$$

where $\langle \dots \rangle$ denotes the thermal average for the interacting system, and $s, s' = \pm$ label the spin indices. In the non-interacting limit ($U = V = J_H = 0$), the spin and charge susceptibilities coincide with the bare susceptibility: $\chi_{\text{spin}} = \chi_{\text{charge}} = \chi^{(0)}$. When interactions are introduced, the random-phase approximation yields the renormalized susceptibilities,

$$\begin{aligned} \chi_{\text{spin}}^{\text{RPA}}(\mathbf{k}, i\omega) &= [I - \chi^{(0)}(\mathbf{k}, i\omega) U^{(s)}]^{-1} \chi^{(0)}(\mathbf{k}, i\omega), \\ \chi_{\text{charge}}^{\text{RPA}}(\mathbf{k}, i\omega) &= [I + \chi^{(0)}(\mathbf{k}, i\omega) U^{(c)}]^{-1} \chi^{(0)}(\mathbf{k}, i\omega), \end{aligned} \quad (13)$$

where the interaction matrices $U^{(s)}$ and $U^{(c)}$ have identical dimensions and are corresponding to the spin and charge channels respectively. For calculation simplicity, we express the susceptibility tensor in matrix form, where rows correspond to orbital indices $l_1 l_2$ and columns to $l_3 l_4$. Figure 7 shows the standard RPA-level Feynman diagrams for both spin and charge susceptibilities. We label the sublattice-orbital basis $\{|A, d_{xz}\rangle, |A, d_{yz}\rangle, |B, d_{xz}\rangle, |B, d_{yz}\rangle\}$ as $\{1, 2, 3, 4\}$. The non-zero elements of the interaction tensor $[U^{(s,c)}]_{l_3 l_4}^{l_1 l_2}$ are then given by:

$$\begin{aligned} [U^{(s)}]_{11}^{11} &= [U^{(s)}]_{22}^{22} = [U^{(s)}]_{33}^{33} = [U^{(s)}]_{44}^{44} = U, \\ [U^{(s)}]_{22}^{11} &= [U^{(s)}]_{11}^{22} = [U^{(s)}]_{44}^{33} = [U^{(s)}]_{33}^{44} = J_H, \\ [U^{(s)}]_{12}^{12} &= [U^{(s)}]_{21}^{21} = [U^{(s)}]_{34}^{34} = [U^{(s)}]_{43}^{43} = J_H, \\ [U^{(s)}]_{21}^{12} &= [U^{(s)}]_{12}^{21} = [U^{(s)}]_{43}^{34} = [U^{(s)}]_{34}^{43} = V, \end{aligned} \quad (14)$$

and

$$\begin{aligned} [U^{(c)}]_{11}^{11} &= [U^{(c)}]_{22}^{22} = [U^{(c)}]_{33}^{33} = [U^{(c)}]_{44}^{44} = U, \\ [U^{(c)}]_{22}^{11} &= [U^{(c)}]_{11}^{22} = [U^{(c)}]_{44}^{33} = [U^{(c)}]_{33}^{44} = 2V - J_H, \\ [U^{(c)}]_{12}^{12} &= [U^{(c)}]_{21}^{21} = [U^{(c)}]_{34}^{34} = [U^{(c)}]_{43}^{43} = J_H, \\ [U^{(c)}]_{21}^{12} &= [U^{(c)}]_{12}^{21} = [U^{(c)}]_{43}^{34} = [U^{(c)}]_{34}^{43} = 2J_H - V. \end{aligned} \quad (15)$$

Magnetic Order from Susceptibility Analysis

To analyze the magnetic order, we first introduce the Matsubara Green's function in momentum space,

$$\mathcal{G}_{l_1, l_3}(\mathbf{k}, \tau) \equiv \langle T_{\tau} S_{l_1}^z(\mathbf{k}, \tau) S_{l_3}^z(-\mathbf{k}, 0) \rangle. \quad (16)$$

Here τ is the imaginary time and T_{τ} represents the time-ordered product of operators and $l_1, l_3 \in \{1, 2, 3, 4\}$ are sublattice-orbital indices. Its Fourier transform gives the static spin susceptibility $\chi_{l_1, l_3}^{(s)}(\mathbf{k})$

$$\begin{aligned} \chi_{l_1, l_3}^{(s)}(\mathbf{k}) &\equiv \mathcal{G}_{l_1, l_3}(\mathbf{k}, i\omega_n = 0), \\ \mathcal{G}_{l_1, l_3}(\mathbf{k}, i\omega_n) &= \int_0^{\beta} d\tau \mathcal{G}_{l_1, l_3}(\mathbf{k}, \tau) e^{i\omega_n \tau}. \end{aligned} \quad (17)$$

Where β is the inverse temperature and $\omega_n = \frac{2\pi n}{\beta}$ is the Matsubara frequency. In the RPA-level $\chi_{l_1, l_3}^{(s)}(\mathbf{k}) \equiv [\chi_{\text{spin}}^{\text{RPA}}(\mathbf{k})]_{l_3, l_3}^{l_1, l_1}$. From linear response theory, as the interaction strength $U \rightarrow U_c^-$, the spin susceptibility matrix $[\chi_{\text{spin}}^{\text{RPA}}(\mathbf{Q})]_{l_3, l_3}^{l_1, l_1}$ diverges at the ordering wave vector \mathbf{Q} . Consequently, the system undergoes a magnetic transition, and the resulting magnetic order is determined by the eigenvector \mathbf{Q} associated with the largest eigenvalue of the susceptibility matrix.

However, when the magnetic order parameter has a more complex structure, this approach requires an additional eigenvector analysis to obtain the correct result [see next section]. In this case, our second criterion for identifying the magnetic order may be more intuitive and reliable. Specifically, as $U \rightarrow U_c^-$, one can directly compare the magnitudes of the susceptibilities corresponding to different magnetic channels at the divergent wave vector \mathbf{Q} [see Eq. (9)], and the system will enter the channel with the most strongly diverging susceptibility.

The Eigen-vector Analysis from Susceptibility

In the main text, we employed a key result: the eigenvector associated with the largest eigenvalue of the static spin susceptibility matrix, $[\chi_{\text{spin}}^{\text{RPA}}(\mathbf{k}, 0)]_{l_3, l_3}^{l_1, l_1}$, directly corresponds to the order parameter of the magnetic phase. To clarify, the orbital indices $l_1 = l_2$ and $l_3 = l_4$ for the general spin susceptibility $[\chi_{\text{spin}}^{\text{RPA}}(\mathbf{k}, 0)]_{l_3, l_4}^{l_1, l_2}$ indicate that this matrix describes spin-spin correlations between these two orbitals (l_1 and l_3). In our work, l_1 represents the basis $\{|A, d_{xz}\rangle, |B, d_{xz}\rangle, |A, d_{yz}\rangle, |B, d_{yz}\rangle\}$. Specifically, the susceptibility matrix captures the linear response of spins in orbital l_1 to perturbations in orbital l_3 (and vice versa), formally defined as:

$$[\chi_{\text{spin}}(\mathbf{k}, \tau)]_{l_3, l_3}^{l_1, l_1} \equiv \frac{1}{2N} \sum_{\mathbf{k}_1 \mathbf{k}_2} \sum_{ss'} \langle T_\tau c_{l_1, s}^\dagger(\mathbf{k}_1, \tau) c_{l_2, s}(\mathbf{k}_1 + \mathbf{k}, \tau) c_{l_3, s'}^\dagger(\mathbf{k}_2 + \mathbf{k}, 0) c_{l_4, s'}(\mathbf{k}_2, 0) \rangle, \quad (18)$$

where $\langle \dots \rangle$ denotes the thermal average for the interacting system, and $s, s' = \pm$ label the spin indices. To account for electron-electron interactions, we compute the spin susceptibility within the random phase approximation (RPA), denoted as $[\chi_{\text{spin}}^{\text{RPA}}(\mathbf{k}, i\omega_n = 0)]_{l_3, l_3}^{l_1, l_1}$ in the static limit. Note that $[\chi_{\text{spin}}^{\text{RPA}}(\mathbf{k}, i\omega_n = 0)]_{l_3, l_3}^{l_1, l_1}$ is a positive definite matrix. The free energy change due to magnetic ordering can be expressed as

$$\Delta F \propto \sum_{\mathbf{k}} \sum_{l_1 l_3} M_{l_1}(\mathbf{k}) [\chi_{\text{spin}}^{\text{RPA}}(\mathbf{k}, 0)]_{l_3, l_3}^{l_1, l_1} M_{l_3}(\mathbf{k}), \quad (19)$$

where $M_{l_1}(\mathbf{k})$ denotes the spin density on the l_1 orbital. We diagonalize the static spin susceptibility matrix,

$$[\chi_{\text{spin}}^{\text{RPA}}(\mathbf{k}, 0)]_{l_3, l_3}^{l_1, l_1} = \sum_{i=1}^4 \lambda_i |\lambda_i\rangle \langle \lambda_i|, \quad (20)$$

where $\lambda_i \geq 0$ are the eigenvalues. Let λ_{\max} be the largest eigenvalue, and decompose the spin density as

$\vec{M}(\mathbf{k}) = M_0 \hat{M}(\mathbf{k})$, where M_0 is the amplitude and $\hat{M}(\mathbf{k})$ is a unit vector. The free energy change is then bounded by: $\Delta F \leq M_0^2 \lambda_{\max}$, with equality achieved when $\hat{M}(\mathbf{k})$ aligns with the eigenvector $|\lambda_{\max}\rangle$,

$$\hat{M}(\mathbf{k}) = |\lambda_{\max}\rangle. \quad (21)$$

This indicates that the system develops a dominant magnetic instability when λ_{\max} diverges at the critical interaction strength $U \rightarrow U_c^-$, marking the transition to long-range magnetic order. Consequently, the corresponding eigenvector $|\lambda_{\max}\rangle$ directly reveals the symmetry and orbital structure of this emergent magnetic phase.

In this work, we investigate six distinct magnetic orders characterized by zero momentum $\mathbf{Q} = 0$. These orders are defined by the following operators: $\mathcal{O}_{1 \rightarrow 6} = \{\tau_z \sigma_0, \tau_x \sigma_0, \tau_z \sigma_z, \tau_0 \sigma_z, \tau_x \sigma_z, \tau_0 \sigma_0\} \otimes s_z$. For clarity, we focus our analysis on two representative cases:

- The first diagonal case: $\{\mathcal{O}_1, \mathcal{O}_3, \mathcal{O}_4, \mathcal{O}_6\}$ for the basis $\{|A, d_{xz}\rangle, |B, d_{xz}\rangle, |A, d_{yz}\rangle, |B, d_{yz}\rangle\}$. In this case, we have

$$\begin{aligned} \mathcal{O}_1 &= \sigma_0 \tau_z s_z, & \mathcal{O}_3 &= \sigma_z \tau_z s_z, \\ \mathcal{O}_4 &= \sigma_z \tau_0 s_z, & \mathcal{O}_6 &= \sigma_0 \tau_0 s_z. \end{aligned} \quad (22)$$

For example, we consider the \mathcal{O}_1 - \mathcal{O}_6 phase transition presented in Fig. 4 in the main text, and use $J_H/U = 0.2$ and $U = 0.99 U_c$. The spin susceptibility matrix $[\chi_{\text{spin}}^{\text{RPA}}(0, 0)]_{l_3, l_3}^{l_1, l_1}$ reads,

$$\begin{pmatrix} 2.45091 & 0.563459 & 1.41528 & 1.18912 \\ 0.563459 & 2.45091 & 1.18912 & 1.41528 \\ 1.41528 & 1.18912 & 2.45091 & 0.563459 \\ 1.18912 & 1.41528 & 0.563459 & 2.45091 \end{pmatrix}, \quad (23)$$

whose eigenvalues and eigenvectors are

$$\lambda_{\max} = 5.61877, \quad |\lambda_{\max}\rangle = (1, 1, 1, 1)^T / 2, \quad (24a)$$

$$\lambda_2 = 2.1136, \quad |\lambda_2\rangle = (1, -1, 1, -1)^T / 2, \quad (24b)$$

$$\lambda_3 = 1.66129, \quad |\lambda_3\rangle = (1, -1, -1, 1)^T / 2, \quad (24c)$$

$$\lambda_4 = 0.409962, \quad |\lambda_4\rangle = (1, 1, -1, -1)^T / 2, \quad (24d)$$

where $|\lambda_{\max}\rangle$ represents the order parameter of the \mathcal{O}_6 phase, while the subdominant eigenvector $|\lambda_2\rangle$ corresponds to the \mathcal{O}_1 phase.

- The second diagonal case: $\{\mathcal{O}_2, \mathcal{O}_4, \mathcal{O}_5, \mathcal{O}_6\}$ for the basis $\{|A, d_+\rangle, |B, d_+\rangle, |A, d_-\rangle, |B, d_-\rangle\}$, where $d_{\pm} = (d_{xz} \pm d_{yz}) / \sqrt{2}$. In this case,

$$\begin{aligned} \mathcal{O}_2 &= \sigma_0 \tau_z s_z, & \mathcal{O}_4 &= \sigma_z \tau_0 s_z, \\ \mathcal{O}_5 &= \sigma_z \tau_z s_z, & \mathcal{O}_6 &= \sigma_0 \tau_0 s_z. \end{aligned} \quad (25)$$

For example, we consider the \mathcal{O}_5 - \mathcal{O}_4 phase transition presented in Fig. 5 in the following section,

and use $J_H/U = 0.2$ and $U = 0.99U_c$. The spin susceptibility matrix $[\chi_{\text{spin}}^{\text{RPA}}(0, 0)]_{l_3 l_3}^{l_1 l_1}$ reads,

$$\begin{pmatrix} 8.00491 & 5.43847 & -7.0189 & -4.99188 \\ 5.43847 & 8.00491 & -4.99188 & -7.0189 \\ -7.0189 & -4.99188 & 8.00491 & 5.43847 \\ -4.99188 & -7.0189 & 5.43847 & 8.00491 \end{pmatrix}, \quad (26)$$

whose eigenvalues and eigenvectors are

$$\lambda_{\max} = 25.4542, \quad |\lambda_{\max}\rangle = (1, 1, -1, -1)^T/2, \quad (27a)$$

$$\lambda_2 = 4.59346, \quad |\lambda_2\rangle = (1, -1, -1, 1)^T/2, \quad (27b)$$

$$\lambda_3 = 1.4326, \quad |\lambda_3\rangle = (1, 1, 1, 1)^T/2, \quad (27c)$$

$$\lambda_4 = 0.539424, \quad |\lambda_4\rangle = (1, -1, 1, -1)^T/2, \quad (27d)$$

where $|\lambda_{\max}\rangle$ represents the order parameter of the \mathcal{O}_4 phase, while the subdominant eigenvector $|\lambda_2\rangle$ corresponds to the \mathcal{O}_5 phase.

The eigenvector analysis of the spin susceptibility matrix directly determines the dominant magnetic order. This conclusion aligns with the divergence behavior (i.e., pronounced divergence rate) observed in the RPA-calculated susceptibility $\chi_{\Gamma, \alpha}^{\text{RPA}}$. Notably, the $\chi_{\Gamma, \alpha}^{\text{RPA}}$ approach offers a more general framework, as it bypasses the need for basis transformations.

Acknowledgments

We thank C. Li, H. K. Jin, Z. M. Pan, M. Zhang, J. Kang and F. Yang for helpful discussions. We thank S. B. Zhang for careful reading of the manuscript. L.H.H. is supported by National Key R&D Program of China (Grant No. 2025YFA1411501), the National Natural Science Foundation of China (Grant Nos. 12561160109, 1257040632), the Fundamental Research Funds for the Central Universities (Grant No. 226-2024-00068). C.L. is supported by the National Natural Science Foundation of China under the Grants No. 12304180.

[1] L. Van Hove, The occurrence of singularities in the elastic frequency distribution of a crystal, *Physical Review* **89**, 1189 (1953).

[2] W. Kohn and J. Luttinger, New mechanism for superconductivity, *Physical Review Letters* **15**, 524 (1965).

[3] C. Honerkamp and M. Salmhofer, Magnetic and superconducting instabilities of the hubbard model at the van hove filling, *Physical Review Letters* **87**, 187004 (2001).

[4] A. Piriou, N. Jenkins, C. Berthod, I. Maggio-Aprile, and Ø. Fischer, First direct observation of the van hove singularity in the tunnelling spectra of cuprates, *Nature communications* **2**, 221 (2011).

[5] Y. Hu, X. Wu, B. R. Ortiz, S. Ju, X. Han, J. Ma, N. C. Plumb, M. Radovic, R. Thomale, S. D. Wilson, *et al.*, Rich nature of van hove singularities in kagome superconductor csv3sb5, *Nature Communications* **13**, 2220 (2022).

[6] J. M. Park, Y. Cao, K. Watanabe, T. Taniguchi, and P. Jarillo-Herrero, Tunable strongly coupled superconductivity in magic-angle twisted trilayer graphene, *Nature* **590**, 249 (2021).

[7] I. Dzyaloshinskii, Superconducting transitions due to van hove singularities in the electron spectrum, *Zhurnal Eksperimental'noi i Teoreticheskoi Fiziki* **93**, 1487 (1987).

[8] R. Markiewicz, Van hove singularities and high-t c superconductivity: a review, *International Journal of Modern Physics B* **5**, 2037 (1991).

[9] R. Radtke and M. Norman, Relation of extended van hove singularities to high-temperature superconductivity within strong-coupling theory, *Physical Review B* **50**, 9554 (1994).

[10] D. Newns, P. Pattnaik, and C. Tsuei, Role of van hove singularity in high-temperature superconductors: Mean field, *Physical Review B* **43**, 3075 (1991).

[11] J. L. McChesney, A. Bostwick, T. Ohta, T. Seyller, K. Horn, J. González, and E. Rotenberg, Extended van hove singularity and superconducting instability in doped graphene, *Phys. Rev. Lett.* **104**, 136803 (2010).

[12] H. Yao and F. Yang, Topological odd-parity superconductivity at type-ii two-dimensional van hove singularities, *Physical Review B* **92**, 035132 (2015).

[13] T. Rice and G. Scott, New mechanism for a charge-density-wave instability, *Physical Review Letters* **35**, 120 (1975).

[14] Y.-P. Lin and R. M. Nandkishore, Complex charge density waves at van hove singularity on hexagonal lattices: Haldane-model phase diagram and potential realization in the kagome metals av 3 sb 5 (a= k, rb, cs), *Physical Review B* **104**, 045122 (2021).

[15] Z. Wu, Y.-M. Wu, and F. Wu, Pair density wave and loop current promoted by van hove singularities in moiré systems, *Physical Review B* **107**, 045122 (2023).

[16] J. González, Charge instabilities near a van hove singularity, *Physical Review B* **63**, 045114 (2001).

[17] S. Cho, H. Ma, W. Xia, Y. Yang, Z. Liu, Z. Huang, Z. Jiang, X. Lu, J. Liu, Z. Liu, *et al.*, Emergence of new van hove singularities in the charge density wave state of a topological kagome metal rbv 3 sb 5, *Physical Review Letters* **127**, 236401 (2021).

[18] J. González, F. Guinea, and M. Vozmediano, Kinematics of electrons near a van hove singularity, *Physical review letters* **84**, 4930 (2000).

[19] M. Fleck, A. M. Oleś, and L. Hedin, Magnetic phases near the van hove singularity in s-and d-band hubbard models, *Physical Review B* **56**, 3159 (1997).

[20] Y.-W. Liu, J.-B. Qiao, C. Yan, Y. Zhang, S.-Y. Li, and L. He, Magnetism near half-filling of a van hove singularity in twisted graphene bilayer, *Physical Review B* **99**, 201408 (2019).

[21] J.-X. Yin, S. S. Zhang, G. Chang, Q. Wang, S. S. Tsirkin, Z. Guguchia, B. Lian, H. Zhou, K. Jiang, I. Belopolski, *et al.*, Negative flat band magnetism in a spin-orbit-coupled correlated kagome magnet, *Nature Physics* **15**, 443 (2019).

[22] M. Vozmediano, J. González, F. Guinea, J. Alvarez, and

B. Valenzuela, Properties of electrons near a van hove singularity, *Journal of Physics and Chemistry of Solids* **63**, 2295 (2002).

[23] A. P. Kampf and A. Katanin, Competing phases in the extended u- v- j hubbard model near the van hove fillings, *Physical Review B* **67**, 125104 (2003).

[24] P. Igoshev, A. Katanin, and V. Y. Irkhin, Magnetic fluctuations and itinerant ferromagnetism in two-dimensional systems with van hove singularities, *Journal of Experimental and Theoretical Physics* **105**, 1043 (2007).

[25] J. Gonzalez, Magnetic and kohn-luttinger instabilities near a van hove singularity: Monolayer versus twisted bilayer graphene, *Physical Review B* **88**, 125434 (2013).

[26] W.-S. Wang, Z.-Z. Li, Y.-Y. Xiang, and Q.-H. Wang, Competing electronic orders on kagome lattices at van hove filling, *Physical Review B—Condensed Matter and Materials Physics* **87**, 115135 (2013).

[27] A. Ziletti, S. M. Huang, D. F. Coker, and H. Lin, Van hove singularity and ferromagnetic instability in phosphorene, *Physical Review B* **92**, 085423 (2015).

[28] W. F. Goh and W. E. Pickett, A mechanism for weak itinerant antiferromagnetism: Mirrored van hove singularities, *Europhysics Letters* **116**, 27004 (2016).

[29] Y. Wang, J.-G. Liu, W.-S. Wang, and Q.-H. Wang, Electronic order near the type-ii van hove singularity in bc 3, *Physical Review B* **97**, 174513 (2018).

[30] Y. Sherkunov and J. J. Betouras, Electronic phases in twisted bilayer graphene at magic angles as a result of van hove singularities and interactions, *Physical Review B* **98**, 205151 (2018).

[31] W. Wu, Z. Shi, M. Ozerov, Y. Du, Y. Wang, X.-S. Ni, X. Meng, X. Jiang, G. Wang, C. Hao, *et al.*, The discovery of three-dimensional van hove singularity, *Nature Communications* **15**, 2313 (2024).

[32] P. Park, B. R. Ortiz, M. Sprague, A. P. Sakhya, S. A. Chen, M. D. Frontzek, W. Tian, R. Sibille, D. G. Mazzzone, C. Tabata, *et al.*, Spin density wave and van hove singularity in the kagome metal ceti3bi4, *Nature Communications* **16**, 4384 (2025).

[33] Y. Yu, H. G. Suh, M. Roig, and D. F. Agterberg, Altermagnetism from coincident van hove singularities: application to κ -cl, *Nature Communications* **16**, 2950 (2025).

[34] S. Giuli, C. Mejuto-Zaera, and M. Capone, Altermagnetism from interaction-driven itinerant magnetism, *Physical Review B* **111**, L020401 (2025).

[35] A. Bose, S. Vadnais, and A. Paramekanti, Altermagnetism and superconductivity in a multiorbital t-j model, *Physical Review B* **110**, 205120 (2024).

[36] T. Li, Spontaneous quantum hall effect in quarter-doped hubbard model on honeycomb lattice and its possible realization in doped graphene system, *Europhysics Letters* **97**, 37001 (2012).

[37] Y. Noda, K. Ohno, and S. Nakamura, Momentum-dependent band spin splitting in semiconducting mno 2: a density functional calculation, *Physical Chemistry Chemical Physics* **18**, 13294 (2016).

[38] M. Naka, S. Hayami, H. Kusunose, Y. Yanagi, Y. Motome, and H. Seo, Spin current generation in organic antiferromagnets, *Nature communications* **10**, 4305 (2019).

[39] K.-H. Ahn, A. Hariki, K.-W. Lee, and J. Kuneš, Antiferromagnetism in ruo2 as d-wave pomeranchuk instability, *Physical Review B* **99**, 184432 (2019).

[40] S. Hayami, Y. Yanagi, and H. Kusunose, Momentum-dependent spin splitting by collinear antiferromagnetic ordering, *journal of the physical society of japan* **88**, 123702 (2019).

[41] L. Šmejkal, R. González-Hernández, T. Jungwirth, and J. Sinova, Crystal time-reversal symmetry breaking and spontaneous hall effect in collinear antiferromagnets, *Science advances* **6**, eaaz8809 (2020).

[42] L.-D. Yuan, Z. Wang, J.-W. Luo, E. I. Rashba, and A. Zunger, Giant momentum-dependent spin splitting in centrosymmetric low-z antiferromagnets, *Physical Review B* **102**, 014422 (2020).

[43] D.-F. Shao, S.-H. Zhang, M. Li, C.-B. Eom, and E. Y. Tsymbal, Spin-neutral currents for spintronics, *Nature Communications* **12**, 7061 (2021).

[44] I. I. Mazin, K. Koepernik, M. D. Johannes, R. González-Hernández, and L. Šmejkal, Prediction of unconventional magnetism in doped fesb2, *Proceedings of the National Academy of Sciences* **118**, e2108924118 (2021).

[45] H.-Y. Ma, M. Hu, N. Li, J. Liu, W. Yao, J.-F. Jia, and J. Liu, Multifunctional antiferromagnetic materials with giant piezomagnetism and noncollinear spin current, *Nature communications* **12**, 2846 (2021).

[46] L.-D. Yuan, Z. Wang, J.-W. Luo, and A. Zunger, Prediction of low-z collinear and noncollinear antiferromagnetic compounds having momentum-dependent spin splitting even without spin-orbit coupling, *Phys. Rev. Mater.* **5**, 014409 (2021).

[47] L. Šmejkal, J. Sinova, and T. Jungwirth, Beyond conventional ferromagnetism and antiferromagnetism: A phase with nonrelativistic spin and crystal rotation symmetry, *Physical Review X* **12**, 031042 (2022).

[48] Z. Feng, X. Zhou, L. Šmejkal, L. Wu, Z. Zhu, H. Guo, R. González-Hernández, X. Wang, H. Yan, P. Qin, *et al.*, An anomalous hall effect in altermagnetic ruthenium dioxide, *Nature Electronics* **5**, 735 (2022).

[49] O. Fedchenko, J. Minár, A. Akashdeep, S. W. D’Souza, D. Vasilyev, O. Tkach, L. Odenbreit, Q. Nguyen, D. Kutnyakov, N. Wind, *et al.*, Observation of time-reversal symmetry breaking in the band structure of altermagnetic ruo2, *Science advances* **10**, eadj4883 (2024).

[50] Z. Lin, D. Chen, W. Lu, X. Liang, S. Feng, K. Yamagami, J. Osiecki, M. Leandersson, B. Thiagarajan, J. Liu, *et al.*, Observation of giant spin splitting and d-wave spin texture in room temperature altermagnet ruo2, *arXiv:2402.04995* (2024).

[51] R. Gonzalez Betancourt, J. Zubáč, R. Gonzalez-Hernandez, K. Geishendorf, Z. Šobáň, G. Springholz, K. Olejník, L. Šmejkal, J. Sinova, T. Jungwirth, *et al.*, Spontaneous anomalous hall effect arising from an unconventional compensated magnetic phase in a semiconductor, *Physical Review Letters* **130**, 036702 (2023).

[52] J. Krempaský, L. Šmejkal, S. D’souza, M. Hajlaoui, G. Springholz, K. Uhlířová, F. Alarab, P. Constantinou, V. Strocov, D. Usanov, *et al.*, Altermagnetic lifting of kramers spin degeneracy, *Nature* **626**, 517 (2024).

[53] S. Lee, S. Lee, S. Jung, J. Jung, D. Kim, Y. Lee, B. Seok, J. Kim, B. G. Park, L. Šmejkal, *et al.*, Broken kramers degeneracy in altermagnetic mnt, *Physical review letters* **132**, 036702 (2024).

[54] T. Osumi, S. Souma, T. Aoyama, K. Yamauchi, A. Honma, K. Nakayama, T. Takahashi, K. Ohgushi, and T. Sato, Observation of a giant band splitting in

altermagnetic mnte, *Physical Review B* **109**, 115102 (2024).

[55] Z. Liu, M. Ozeki, S. Asai, S. Itoh, and T. Masuda, Chiral split magnon in altermagnetic mnte, *Physical Review Letters* **133**, 156702 (2024).

[56] S. Reimers, L. Odenbreit, L. Šmejkal, V. N. Strocov, P. Constantinou, A. B. Hellenes, R. Jaeschke Ubiergo, W. H. Campos, V. K. Bharadwaj, A. Chakraborty, et al., Direct observation of altermagnetic band splitting in crsb thin films, *Nature Communications* **15**, 2116 (2024).

[57] J. Ding, Z. Jiang, X. Chen, Z. Tao, Z. Liu, T. Li, J. Liu, J. Sun, J. Cheng, J. Liu, et al., Large band splitting in g-wave altermagnet crsb, *Physical Review Letters* **133**, 206401 (2024).

[58] G. Yang, Z. Li, S. Yang, J. Li, H. Zheng, W. Zhu, Z. Pan, Y. Xu, S. Cao, W. Zhao, et al., Three-dimensional mapping of the altermagnetic spin splitting in crsb, *Nature Communications* **16**, 1442 (2025).

[59] F. Zhang, X. Cheng, Z. Yin, C. Liu, L. Deng, Y. Qiao, Z. Shi, S. Zhang, J. Lin, Z. Liu, et al., Crystal-symmetry-paired spin-valley locking in a layered room-temperature metallic altermagnet candidate, *Nature Physics* , 1 (2025).

[60] B. Jiang, M. Hu, J. Bai, Z. Song, C. Mu, G. Qu, W. Li, W. Zhu, H. Pi, Z. Wei, et al., Discovery of a metallic room-temperature d-wave altermagnet kv2se2o, *arXiv preprint arXiv:2408.00320* (2024).

[61] B. Jiang, M. Hu, J. Bai, Z. Song, C. Mu, G. Qu, W. Li, W. Zhu, H. Pi, Z. Wei, et al., A metallic room-temperature d-wave altermagnet, *Nature Physics* , 1 (2025).

[62] Y. Xu, H. Zhang, M. Feng, and F. Tian, Electronic structure, magnetic transition, and fermi surface instability of the room-temperature altermagnet kv 2 se 2 o, *Physical Review B* **112**, 125141 (2025).

[63] L. Yang, Y.-Y. Jiang, X.-Y. Guo, S.-H. Zhang, R.-C. Xiao, W.-J. Lu, L. Wang, Y.-P. Sun, E. Y. Tsymbal, and D.-F. Shao, Interface-controlled antiferromagnetic tunnel junctions, *Newton* (2025).

[64] S.-S. Zhang, Z.-A. Wang, B. Li, Y.-Y. Jiang, S.-H. Zhang, R.-C. Xiao, L.-X. Liu, X. Luo, W.-J. Lu, M. Tian, et al., X-type stacking in cross-chain antiferromagnets, *Newton* **1** (2025).

[65] L. Šmejkal, J. Sinova, and T. Jungwirth, Emerging research landscape of altermagnetism, *Physical Review X* **12**, 040501 (2022).

[66] R. González-Hernández, L. Šmejkal, K. Výborný, Y. Yaghagi, J. Sinova, T. Jungwirth, and J. Železný, Efficient electrical spin splitter based on nonrelativistic collinear antiferromagnetism, *Physical Review Letters* **126**, 127701 (2021).

[67] L. Šmejkal, A. B. Hellenes, R. González-Hernández, J. Sinova, and T. Jungwirth, Giant and tunneling magnetoresistance in unconventional collinear antiferromagnets with nonrelativistic spin-momentum coupling, *Physical Review X* **12**, 011028 (2022).

[68] L. Guo, S. Hu, X. Gu, R. Zhang, K. Wang, W. Yan, and X. Sun, Emerging spintronic materials and functionalities, *Advanced Materials* **36**, 2301854 (2024).

[69] D.-F. Shao and E. Y. Tsymbal, Antiferromagnetic tunnel junctions for spintronics, *npj Spintronics* **2**, 13 (2024).

[70] C. Song, H. Bai, Z. Zhou, L. Han, H. Reichlova, J. H. Dil, J. Liu, X. Chen, and F. Pan, Altermagnets as a new class of functional materials, *Nature Reviews Materials* , 1 (2025).

[71] J. E. Hirsch, Spin-split states in metals, *Phys. Rev. B* **41**, 6820 (1990).

[72] C. Wu and S.-C. Zhang, Dynamic generation of spin-orbit coupling, *Physical review letters* **93**, 036403 (2004).

[73] C. Wu, K. Sun, E. Fradkin, and S.-C. Zhang, Fermi liquid instabilities in the spin channel, *Physical Review B* **75**, 115103 (2007).

[74] H. Ikeda and Y. Ohashi, Theory of unconventional spin density wave: A possible mechanism of the micromagnetism in u-based heavy fermion compounds, *Phys. Rev. Lett.* **81**, 3723 (1998).

[75] L. Bai, W. Feng, S. Liu, L. Šmejkal, Y. Mokrousov, and Y. Yao, Altermagnetism: Exploring new frontiers in magnetism and spintronics, *Advanced Functional Materials* **34**, 2409327 (2024).

[76] S. S. Fender, O. Gonzalez, and D. K. Bediako, Altermagnetism: A chemical perspective, *Journal of the American Chemical Society* **147**, 2257 (2025).

[77] R. M. Fernandes, V. S. de Carvalho, T. Birol, and R. G. Pereira, Topological transition from nodal to nodeless zeeman splitting in altermagnets, *Phys. Rev. B* **109**, 024404 (2024).

[78] Q. Liu, X. Dai, and S. Blügel, Different facets of unconventional magnetism, *Nature Physics* , 1 (2025).

[79] V. Leeb, A. Mook, L. Šmejkal, and J. Knolle, Spontaneous formation of altermagnetism from orbital ordering, *Physical Review Letters* **132**, 236701 (2024).

[80] R. He, D. Wang, N. Luo, J. Zeng, K.-Q. Chen, and L.-M. Tang, Nonrelativistic spin-momentum coupling in antiferromagnetic twisted bilayers, *Phys. Rev. Lett.* **130**, 046401 (2023).

[81] Y. Liu, J. Yu, and C.-C. Liu, Twisted magnetic van der waals bilayers: an ideal platform for altermagnetism, *Physical Review Letters* **133**, 206702 (2024).

[82] L. Šmejkal, Altermagnetic multiferroics and altermagnetoelectric effect, *arXiv preprint arXiv:2411.19928* (2024).

[83] X. Duan, J. Zhang, Z. Zhu, Y. Liu, Z. Zhang, I. Žutić, and T. Zhou, Antiferroelectric altermagnets: Antiferroelectricity alters magnets, *Physical Review Letters* **134**, 106801 (2025).

[84] M. Gu, Y. Liu, H. Zhu, K. Yananose, X. Chen, Y. Hu, A. Stroppa, and Q. Liu, Ferroelectric switchable altermagnetism, *Physical Review Letters* **134**, 106802 (2025).

[85] A. Chakraborty, R. González Hernández, L. Šmejkal, and J. Sinova, Strain-induced phase transition from antiferromagnet to altermagnet, *Physical Review B* **109**, 144421 (2024).

[86] X. Zhu, X. Huo, S. Feng, S.-B. Zhang, S. A. Yang, and H. Guo, Design of altermagnetic models from spin clusters, *Physical Review Letters* **134**, 166701 (2025).

[87] Z. Li, X. Ma, S. Wu, H.-Q. Yuan, J. Dai, and C. Cao, Pressure induced altermagnetism in layered ternary iron-selenides, *arXiv:2503.11228* (2025).

[88] T. A. Maier and S. Okamoto, Weak-coupling theory of neutron scattering as a probe of altermagnetism, *Physical Review B* **108**, L100402 (2023).

[89] M. Roig, A. Kreisel, Y. Yu, B. M. Andersen, and D. F. Agterberg, Minimal models for altermagnetism, *Phys.*

Rev. B **110**, 144412 (2024).

[90] P. Das, V. Leeb, J. Knolle, and M. Knap, Realizing altermagnetism in fermi-hubbard models with ultracold atoms, *Physical Review Letters* **132**, 263402 (2024).

[91] T. Sato, S. Haddad, I. C. Fulga, F. F. Assaad, and J. van den Brink, Altermagnetic anomalous hall effect emerging from electronic correlations, *Phys. Rev. Lett.* **133**, 086503 (2024).

[92] M. Zhao, W.-W. Yang, X. Guo, H.-G. Luo, and Y. Zhong, Altermagnetism in heavy-fermion systems: Mean-field study on the kondo lattice, *Phys. Rev. B* **111**, 085145 (2025).

[93] L. Camerano, A. O. Fumega, J. L. Lado, A. Stroppa, and G. Profeta, Multiferroic nematic d-wave altermagnetism driven by orbital-order on the honeycomb lattice, *npj 2D Materials and Applications* **9**, 75 (2025).

[94] C. Li and et al., Spontaneous nematic altermagnetism, In preparation.

[95] This corresponds to the $\mathbf{Q} = 0$ magnetic order in use of unit cell gauge formed by combining the two sublattices.

[96] T. Jungwirth, J. Sinova, R. M. Fernandes, Q. Liu, H. Watanabe, S. Murakami, S. Nakatsuji, and L. Šmejkal, Symmetry, microscopy and spectroscopy signatures of altermagnetism, *Nature* **649**, 837 (2026).

[97] C. Castellani, C. Natoli, and J. Ranninger, Magnetic structure of $\text{v}2\text{o}3$ in the insulating phase, *Physical Review B* **18**, 4945 (1978).

[98] Z.-M. Wang, Y. Zhang, S.-B. Zhang, J.-H. Sun, E. Dagotto, D.-H. Xu, and L.-H. Hu, Spin-orbital altermagnetism, *Phys. Rev. Lett.* **135**, 176705 (2025).

[99] D. Scalapino, E. Loh Jr, and J. Hirsch, d -wave pairing near a spin-density-wave instability, *Phys. Rev. B* **34**, 8190 (1986).

[100] T. Moriya, *Spin fluctuations in itinerant electron magnetism* Vol. 56 (Springer Science & Business Media, 2012).

[101] D. Hamann, Properties of the renormalized random-phase approximation for dilute magnetic alloys, *Physical Review* **186**, 549 (1969).

[102] M. Zhang, H. Sun, Y.-B. Liu, Q. Liu, W.-Q. Chen, and F. Yang, Spin-density wave and superconductivity in $\text{la}4\text{ni}3\text{o}10$ under ambient pressure, *Physical Review B* **111**, 144502 (2025).

[103] C. Lu, C. Cao, H. Yuan, P. Coleman, and L.-H. Hu, Breakdown of stoner ferromagnetism by intrinsic altermagnetism, *arXiv preprint arXiv:2510.00614* (2025).

[104] C. Lu, C. Li, C. Cao, H. Yuan, F.-C. Zhang, and L.-H. Hu, Inter-orbital spin-triplet superconductivity from altermagnetic fluctuations, *arXiv preprint arXiv:2510.19083* (2025).

[105] B. Pandey, Y. Zhang, N. Kaushal, R. Soni, L.-F. Lin, W.-J. Hu, G. Alvarez, and E. Dagotto, Origin of the magnetic and orbital ordering in $\alpha\text{-sr}2\text{cr}04$, *Physical Review B* **103**, 045115 (2021).

[106] M.-C. Lee, C. Occhialini, J. Li, Z. Zhu, N. S. Sirica, L. Mix, S. Kim, D. A. Yarotski, R. Comin, and R. P. Prasankumar, Ultrafast signatures of spin and orbital order in antiferromagnetic $\alpha\text{-sr}2\text{cro}4$, *Communications Physics* **5**, 335 (2022).

[107] C. Autieri, Antiferromagnetic and xy ferro-orbital order in insulating $\text{sr}ruo3$ thin films with sro termination, *Journal of Physics: Condensed Matter* **28**, 426004 (2016).

[108] R. Shiina, F. Mila, F.-C. Zhang, and T. Rice, Atomic spin, molecular orbitals, and anomalous antiferromagnetism in insulating $\text{v}2\text{o}3$, *Physical Review B* **63**, 144422 (2001).

[109] T. Maitra and R. Valenti, Orbital order in $\text{znv}2\text{o}4$, *Physical review letters* **99**, 126401 (2007).

[110] R. J. Goff, A. J. Williams, and J. P. Attfield, Spin, charge, and orbital order in $\text{mn}2\text{obo}3$, *Physical Review B—Condensed Matter and Materials Physics* **70**, 014426 (2004).

[111] M. v. Zimmermann, J. Hill, D. Gibbs, M. Blume, D. Casa, B. Keimer, Y. Murakami, Y. Tomioka, and Y. Tokura, Interplay between charge, orbital, and magnetic order in $\text{pr}1\text{-x ca x mno}3$, *Physical Review Letters* **83**, 4872 (1999).

[112] H. Ehrke, R. Tobey, S. Wall, S. Cavill, M. Först, V. Khanna, T. Garl, N. Stojanovic, D. Prabhakaran, A. Boothroyd, et al., Photoinduced melting of antiferromagnetic order in $\text{la}0.5\text{sr}1.5\text{mno}4$ measured using ultrafast resonant soft x-ray diffraction, *Physical review letters* **106**, 217401 (2011).

[113] P. Radaelli, D. Cox, M. Marezio, and S. Cheong, Charge, orbital, and magnetic ordering in $\text{la}0.5\text{ca}0.5\text{mno}3\text{s}$, *Physical Review B* **55**, 3015 (1997).